AGU ADVANCING EARTH AND SPACE SCIENCE

Earth and Space Science

RESEARCH ARTICLE
10.1029/2021EA002036

Evidence for Short Temporal Atmospheric Variations Observed by Infrasonic Signals: 1. The Troposphere

G. Averbuch[1], M. Ronac-Giannone[1], S. Arrowsmith[1], and J. F. Anderson[2]

[1]Roy M. Huffington Department of Earth Sciences, Southern Methodist University, Dallas, TX, USA, [2]Department of Geosciences, Boise State University, Boise, ID, USA

Key Points:

- Evidence for temporal (minute-scale) variability of the lower troposphere is observed by infrasound
- Short temporal dynamics affects infrasonic phases, waveforms, propagation time, and energy

Correspondence to:

G. Averbuch,
gaverbuch@smu.edu

Citation:

Averbuch, G., Ronac-Giannone, M., Arrowsmith, S., & Anderson, J. F. (2022). Evidence for short temporal atmospheric variations observed by infrasonic signals: 1. The troposphere. *Earth and Space Science*, *9*, e2021EA002036. https://doi.org/10.1029/2021EA002036

Received 21 SEP 2021
Accepted 20 JAN 2022

Author Contributions:

Conceptualization: G. Averbuch
Data curation: G. Averbuch, M. Ronac-Giannone
Investigation: G. Averbuch, M. Ronac-Giannone, S. Arrowsmith
Methodology: G. Averbuch, S. Arrowsmith
Resources: S. Arrowsmith, J. F. Anderson
Supervision: S. Arrowsmith
Writing – original draft: G. Averbuch
Writing – review & editing: G. Averbuch

Abstract Infrasound monitoring is used in the forensic analysis of events, studying the physical processes of sources of interest, and probing the atmosphere. The dynamical nature of the atmosphere and the use of infrasound as a forensic tool lead to the following questions; (1) what is the timescale of atmospheric variability that affects infrasonic signals? (2) how do infrasound signals vary as a function of time? This study addresses these questions by monitoring a repetitive infrasound source and its corresponding tropospheric returns 54 km away. Source-receiver empirical Green's functions are obtained every 20 s and used to demonstrate the effect of atmospheric temporal variability on infrasound propagation. In addition, observations are compared to predicted simulated signals based on realistic atmospheric conditions. Based on 127 events over 3 days, it is shown that infrasound properties change within tens of seconds. Particularly, phases can appear and disappear, the propagation time varies, and the signals' energy fluctuates. Such variations are attributed to changes in temperatures and winds. Furthermore, atmospheric models can partly explain the observed changes. Therefore, this study highlights the potential of high temporal infrasound-based atmospheric sounding.

1. Introduction

Infrasonic waves are low-frequency sound waves (0.02–20 Hz) that propagate in the atmosphere, and their sources can be both natural and anthropogenic (Le Pichon et al., 2010). The propagation of infrasound in the atmosphere is affected by the spatial and temporal variations of temperature and wind. In particular, the combination of the temperature and winds in the direction of propagation (along-track winds) forms the effective speed of sound profile, $c_{\text{eff}}(z$; Godin, 2002). This profile is used to approximate how sound propagates in the atmosphere; a decrease or increase of $c_{\text{eff}}(z)$ with height, z, leads to upward or downward refraction, respectively. Therefore, acoustic waveguides that trap acoustic energy are formed depending on the atmospheric conditions.

There are three distinct acoustic waveguides in the atmosphere; the tropospheric, stratospheric, and thermospheric waveguides. These waveguides are usually bounded at ground level due to the rigid boundary at the atmosphere's interface with the ocean and solid Earth. The troposphere extends from the Earth's surface up to the tropopause (10–12 km); it is characterized by a decrease in temperature. A decrease in temperature also implies a decrease in the speed of sound. Therefore, the troposphere typically cannot trap acoustic energy and act as a waveguide based only on temperature. However, due to the strong tropospheric jet stream, the tropospheric waveguide is formed. This waveguide facilitates infrasound propagation (Evers & Haak, 2010). At altitudes between 10 and 50 km, a temperature increase in the stratosphere, combined with the stratospheric jet, forms the stratospheric waveguide. In the northern hemisphere, the stratospheric winds usually flow westward in the summer and eastward in the winter. However, events of sudden stratospheric warming lead to temporary inversion of the stratospheric winds' direction (Butler et al., 2017). Therefore, the stratospheric waveguide supports propagation in different directions depending on the time of the year. In the thermosphere (above 90 km), a rapid increase in temperature forms the thermospheric waveguide. Acoustic waves experience high attenuation in the thermosphere due to its low density (Smets & Evers, 2014; Sutherland & Bass, 2004). In addition, elevated waveguides are also possible. These waveguides are characterized by low c_{eff} altitudes bounded below and above by higher c_{eff} regions. The combination of the low-frequency content and atmospheric waveguides facilitates long-range infrasound propagation and allows its detection by ground-based arrays (Waxler & Assink, 2019).

Infrasonic signals are detected by arrays of microbarometers that measure atmospheric pressure fluctuations. The usage of arrays allows utilizing array processing techniques that yield valuable parameters; first, the single-channel signal-to-noise ratio (SNR), which is used as a detection criterion (Averbuch et al., 2018; Le Pichon

et al., 2009). Second, the detected wave's slowness vector (inverse of the phase velocity). The slowness vector is used to estimate the back azimuth, which is the direction from which the wavefront arrived at the array, and the apparent velocity, which indicates the wave's inclination angle (Olson, 2004; Shumway, 1971). Back azimuth values may deviate from the actual azimuth toward the source due to cross-track winds (normal to the plane of propagation; Evers & Haak, 2005; Ottemöller & Evers, 2008; Smets et al., 2016). In addition, array processing techniques increase SNR values, which improves signal detection by suppressing incoherent background noise and suppressing coherent signals impinging from other directions of arrival than the one of interest.

The efficient propagation of infrasound in the atmosphere combined with array processing techniques makes infrasound monitoring useful in two ways. First, infrasound is used to study sources of infrasound such as ocean waves (Arrowsmith, 2018; Averbuch et al., 2019; Brekhovskikh et al., 1973; De Carlo et al., 2021; Posmentier, 1967; Smets & Evers, 2014; Vorobeva et al., 2021; Waxler & Gilbert, 2006), volcanic eruptions (Anderson, Johnson, Steele, et al., 2018; Fee & Garcés, 2007; Smets et al., 2016), earthquakes (Donn & Posmentier, 1964; Evers et al., 2014; Shani-Kadmiel et al., 2018, 2021), sprites (Applbaum et al., 2020), and explosions (Assink et al., 2016, 2018; Pilger et al., 2021). Especially, infrasound is one of four technologies used to verify the comprehensive nuclear-test-ban treaty (Dahlman et al., 2009). Second, infrasound can be used to probe the atmosphere. It has been done by: (1) quantifying atmospheric winds based on back azimuth, apparent velocity, and travel time variations (Assink et al., 2012; Blixt et al., 2019; Diamond, 1964), (2) using back azimuth and apparent velocity values as constraints for probabilistic inversion (Assink et al., 2013; Drob et al., 2009; Lalande et al., 2012; Le Pichon et al., 2005; Smets et al., 2016; Vanderbecken et al., 2020; Vera Rodriguez et al., 2020), (3) infrasound ambient noise interferometry (Fricke et al., 2014; Haney, 2009; Ortiz et al., 2021), and (4) assimilation of infrasound data (Amezcua & Barton, 2021; Amezcua et al., 2020).

Since the atmosphere is dynamic, infrasound propagation conditions are continuously changing. For example, Ortiz et al. (2021) observe variations in the atmospheric properties (over several kilometers) over a timescale of 30 min. In addition, atmospheric soundings based on long-range propagation (hundreds of kilometers) show temporal variations in the observed back azimuth and apparent velocity in timescales of hours; these observations also deviate from the predicted values by several degrees and tens of meters per second (Smets et al., 2016; Vanderbecken et al., 2020). Based on an active source, Talmadge et al. (2008) show how the length of higher-frequency (up to 200 Hz) signals that propagated a distance of 2 km in the nocturnal boundary layer changes over 15–20 min. Similar timescale effects were observed by Chunchuzov and Kulichkov (2019) for stratospheric returns 300 km from the source. Therefore, the timescales at which changes in the atmosphere affect infrasound propagation are essential; specifically, when infrasound is used to detect, locate, and study a particular event (Arrowsmith et al., 2021). Then, propagation models are often used to explain the observations by simulating infrasound propagation through realistic atmospheric conditions, that is, temperature and winds (Applbaum et al., 2020; Assink et al., 2016, 2018; Evers et al., 2018; Fee et al., 2013; Shani-Kadmiel et al., 2018, 2021). The atmospheric conditions are retrieved from weather prediction models or atmospheric reanalysis models operated by (but not only) the European Centre for Medium-Range Weather Forecasts (ECMWF), North American Mesoscale Model (NAM), and NASA's Global Modeling and Assimilation Office (NASA-GMAO). Depending on the model, estimates of the atmospheric state are issued at most every hour, and sometimes every 3, 6, and 12 hr (Drob et al., 2003; Schwaiger et al., 2019; Smets et al., 2015, 2016). The dynamical nature of the atmosphere and the use of infrasound as a forensic tool lead to the following questions:

1. What is the timescale of infrasound decorrelation?
2. How sensitive are different features (e.g., traveltime, amplitude, phases, back azimuth, apparent velocity) to short temporal dynamics?
3. Can atmospheric specifications accurately explain our observations?
4. Can we link variations of infrasound signals to a specific atmospheric phenomenon?

In what follows, using a specifically designed measurement campaign, we will try to answer these questions for infrasound propagation in the tropospheric waveguide. The campaign consists of acoustic measurements of a repeating source and its corresponding infrasound arrivals at a distance of 54 km. Based on these measurements, the source-receiver empirical Green's functions are retrieved, and the effect of temporal atmospheric variations on infrasonic signals is demonstrated. These effects include time evolution of the retrieved phases (decorrelation of the signals over time), decreased propagation time, and variations of the signals' energy. Section 2 describes

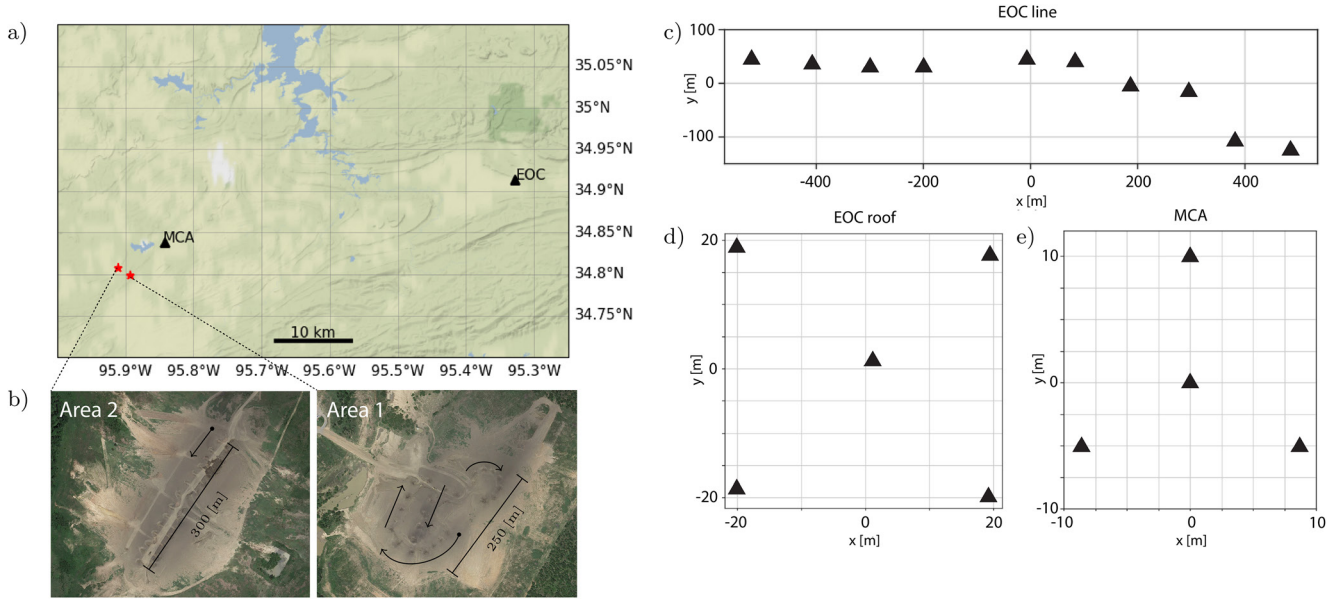

Figure 1. Frame (a) shows the map of the campaign area, detonation sites, and array locations. The two red stars correspond to areas 1 and 2, and the black triangles represent the locations of MCA, and Eastern Oklahoma College (EOC) arrays. Frame (b) shows areas 1 and 2. The black arrows mark the detonation sequence. Frames (c–e) show the arrays configurations of EOC line, EOC roof, and MCA arrays, respectively.

the data acquisition. The methods used to process the data and quantify the temporal variability are described in Section 3. These methods include beamforming, empirical Green's function retrieval, cross correlation, and wave-propagation modeling. Sections 4–6 consist of the results, discussion, and conclusions, respectively.

2. Data Acquisition

This study is based on a repetitive, active source located at the McAlester Army Ammunition Plant (McAAP), Oklahoma, USA. The data acquisition took place between January 13, 2021, and March 2, 2021, and the location is motivated by Carmichael et al. (2021) who studied seismoacoustic signals originated from the same source. One of McAAP's missions is to destroy old ammunition by detonating it. For that, two areas (denoted by 1 and 2) with 26 pits each are used (Figure 1). In Area 1, the pits are arranged in a circular shape; in Area 2, they are located along a straight line. Almost every day, the pits are filled up with old ammunition and detonated in 20-s intervals. Every set (from each area) starts with two test detonations, followed by a 1-min break, and continues with the remaining 24 detonations. There is an approximately 2-min break between each set, and on some days, there is only one set of detonations.

A four-element array (MCA) was deployed approximately seven kilometers from the detonation sites. This array aims to act as a source reference (further explanation is provided in Section 3.2). In order to detect tropospheric signals, two arrays were deployed east of McAAP at the Eastern Oklahoma College (EOC) at Wilburton, Oklahoma, USA. EOC is at a distance of 54 km and an azimuth of 77° from McAAP. The arrays consisted of a five-element roof array (EOCR) and a 10-element 1-km line array (EOCL). The distance between the centers of the arrays is 200 m. Figure 1 shows the locations and configurations of the arrays.

MCA and EOCR consist of Hyperion IFS-3000 sensors combined with Nanometric's Pegasus data logger, sampling at 100 and 40 Hz, respectively. The IFS-3000 has a flat frequency response from 0.01 to 100 Hz. EOCL array comprises Gem infrasound sensors that record at 100 Hz and have a flat response between 0.05 and 25 Hz (Anderson, Johnson, Bowman, & Ronan, 2018). Out of the acquisition period, we focus on 3 days (January 20 and February 2 and 5, 2021) consisting of 127 events with high SNR, where different behaviors of the signals characterize each day.

3. Methods

3.1. Beamforming

Delay-and-sum beamforming is an array processing technique that estimates the recorded waves' parameters. The method assumes that the signal of interest is coherent across the array while the background (wind) noise is incoherent. Consequently, a signal is enhanced while background noise is suppressed. In the case of concurrent sources, beamforming can also enhance signals arriving from a direction of interest while suppressing coherent signals impinging from other directions. Combined with Fisher statistics, it provides the back azimuth, apparent velocity, and SNR (Melton & Bailey, 1957). Based on these parameters, one can reconstruct the array's best beam. The best beam is the back azimuth and apparent velocity combination that yields the delay-and-sum signal with the highest possible SNR. Implementations of the method exist both in time domain (Assink et al., 2016; Smets & Evers, 2014) and frequency domain (Averbuch, 2021; den Ouden et al., 2020; Smart & Flinn, 1971).

In this study, time domain beamforming is used for the array analysis. We utilize the code used by Shani-Kadmiel et al. (2021). Data are upsampled to 200 Hz, bandpass-filtered between 1 and 10 Hz, and a 15-s sliding window is used with an overlap of 95%. The grid resolution was set to apparent velocity resolution of 2 m/s and azimuthal resolution of 1°. Although the detected signals contain lower and higher-frequency components, these processing parameters yield the highest SNR values.

EOC beamforming results show some variability in both back azimuth and apparent velocity (Appendix A). These results may be attributed to both atmospheric variability and the different locations of areas 1 and 2. However, the variance of the array resolution is larger than the observed variability (Appendix A). Therefore, no additional emphasis will be given to these parameters. Nonetheless, the arrays' best beams are used to obtain the atmosphere's empirical Green's functions between MCA and EOC (Section 3.2). Using the best beam (and not a single-station recording) minimizes the effect of incoherent local noise on the empirical Green's functions. The differences between the best beams from EOCR and EOCL are negligible. Therefore, the EOCR best beams will be used throughout the rest of the analysis. For simplicity, EOCR will be referred to as EOC.

3.2. Empirical Green's Functions and Cross Correlation

For the next step, the best beams are used to obtain the empirical Green's function (EGF) between MCA and EOC. Following the convolution theorem, one can describe an observed signal as a convolution between the Green's function (between the source and receiver) and a source-time function (Desanto, 1992). Here, MCA best beams are used as references for the source. Despite the distance from the detonation areas, the region is flat, and no signal modulation is expected. The only expected difference is in amplitude. Deploying another reference sensor 4 km north of the pits supports this hypothesis (due to access problems, this test was possible after the time period of this campaign. Further information can be found in Appendix B). In addition, similar observations by Kim et al. (2018) show that for local infrasound propagation, no significant modulation of the signal is observed up to 6 km from the source in an area without extreme topography. Furthermore, cross-correlation values of the detonations' signals at frequencies between 1 and 10 Hz are relatively high. The high coefficients suggest that the area and pit configuration have little effect on the waveforms at these frequencies. To further support these observations, broadband simulations (Section 3.3) at different azimuths show that for frequencies below 15 Hz and propagation distance below 10 km, there is no multipathing or change of the signal waveform (not shown here). The simulations show that the waveforms vary only in amplitude.

The atmosphere's EGF is obtained by deconvolving the source reference (MCA best beam) from the observed signal (EOC best beam). It is done in the frequency domain by dividing the spectral content of the observed signal by the source reference. In order to avoid artifacts, we made sure that the source spectral content is not zero (otherwise, a division by zero or by a small number can excite spurious frequencies). Doing this for each detonation removes source effects and provides us with the atmosphere's EGFs as a function of time. Implicitly, the EGF series describes how the medium changes over the time of detonations. In order to represent how variations in the medium affect infrasound signals, synthetic signals are obtained by convolving the EGFs with a Ricker wavelet (source-time function) with a 3 Hz central frequency; this source-time function has a frequency spectrum that matches the analyzed data's 1–10 Hz frequency band. The EGF-base synthetics will be denoted by EGFS. Since

subtle source effects are thus removed, any variation in the EGFS (amplitudes, phases, waveforms, and propagation time) is associated with variations in the atmosphere.

In order to show the signals' change rate, the EGFS are cross-correlated with each other. The first signal from each day and set is used as a reference. Cross correlation yields the correlation coefficient and the time delay between two signals. Therefore, applying it to the data provides the variations of correlation coefficient and time delay over time. These time series describe the timescale of infrasound decorrelation due to atmospheric variability and the variations in the propagation time. It will be shown that the time delay values are affected by both the source location (distance between pits) and the atmosphere.

3.3. Green's Function Parabolic Equation

In comparison to the EGFS, we use the parabolic wave equation to simulate acoustic signals from McAAp to EOC through realistic atmospheric conditions. The parabolic form of the wave equation is a one-way wave equation that describes the propagation of an outgoing wavefield, that is, it does not account for back-scattering (Collins & Siegmann, 2019). Green's function Parabolic Equation (GFPE) is a numerical wave-propagation method that is based on the split-step solution (Gilbert, 2016). Generally, the propagation in each range step is split into two; first, the wavefield is propagated over a homogeneous half-space. This step is based on the acoustic Green's function for homogeneous medium in the wavenumber domain. Second, the propagated field is multiplied by a phase corrector that accounts for the variations in the velocity profile (Feit & Fleck, 1978; Thomson & Chapman, 1983). A known limitation of the GFPE split-step method is the restriction to narrow-angle propagation. This constraint prevents simulating long-range stratospheric and thermospheric propagation with the GFPE. However, this study focuses on low-altitude tropospheric propagation, characterized by low propagation angles (<12°). Therefore, the narrow-angle restriction is satisfied.

The simulations are based on realistic atmospheric profiles that contain vertical variability of density, temperature, and winds; these are based on NASA's MERRA2 product (Gelaro et al., 2017). For convenience the profiles are retrieved via the ground-to-space (G2S) (Drob, 2019; Drob et al., 2003) experimental prototype server of NCPA (http://130.74.32.249/). The atmospheric profiles were extracted every 5 km between McAAP (midpoint between areas 1 and 2) and EOC (distance of 54 km) for each day at 16:34, 17:34, and 18:34 UTC (10:34 a.m., 11:34 a.m., and 12:34 p.m. local time). At each location, the c_{eff} profile was computed. No significant change was observed between the c_{eff} profile along the propagation path. Therefore, the average c_{eff} profile was used for the simulations. Narrowband simulations (GFPE-N) at 10 Hz are used to indicate the propagation paths in the atmosphere each day at 17:34 UTC. These results are presented in terms of transmission loss (TL), which describes the decrease in the wave intensity (Jensen et al., 2011); it can also be understood as the signal attenuation in dB. Broadband simulations (GFPE-B) are used to show the evolution of the predicted waveform over time. For that, simulations are performed three times per day. A Ricker wavelet with a 3 Hz central frequency is used for the simulations (same as the EGFS). Cross correlation is used to compare signals from the GFPE-B and the EGFS. The pair with the highest correlation coefficient will be presented.

4. Results

4.1. January 20, 2021

Figures 2a and 2b show the time evolution of the EGFS. The signals start with two phases at 140 and 142 s. During the first set, the amplitude of the first phase decreases while the second phase's waveforms are slowly changing. On the second set, only one clear phase is apparent. There is a two-second difference in the arrival time between the two sets. It is attributed to the approximately 700 m difference between areas 1 and 2 (in the direction of propagation). In both sets, the correlations coefficients decrease within tens of seconds (Figures 2c and 2d). However, they change at different rates. In addition, variations in the arrival time between the shots are also observable (Figures 2e and 2f). The periodic-like shape of the time delays in the first set results from the semicircular shape of area 1 and the steady increase in the second set can partly be explained by the linear shape of area 2. The atmosphere also affects these values, and it will be further discussed in Section 5.

The atmospheric conditions for this day predict a low-tropospheric waveguide bounded between the ground and 2 km (Figure 3a). The waveguide is formed by low-altitude winds in the along-track propagation directions.

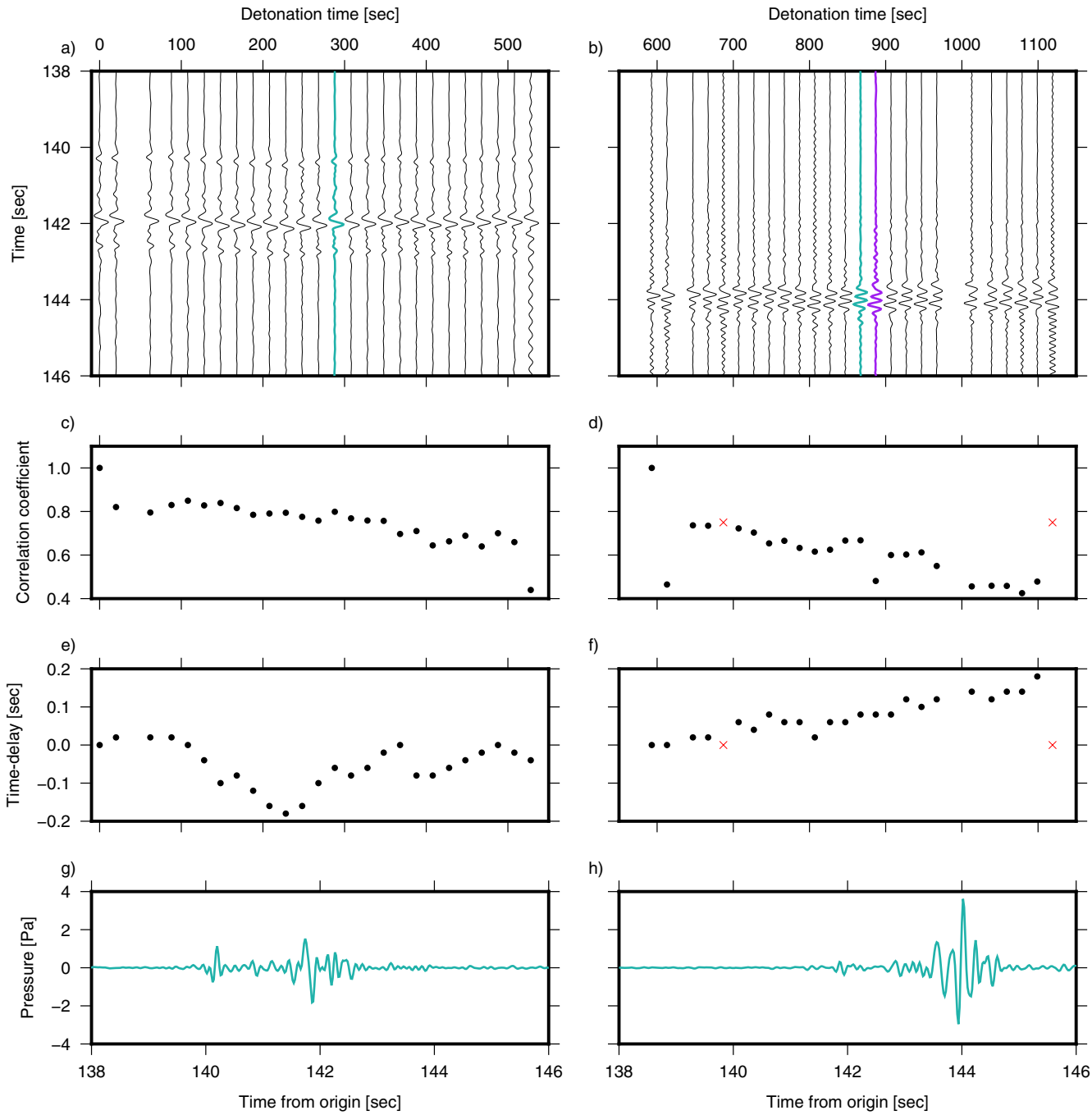

Figure 2. Empirical Green's functions based synthetics waveforms and their correlation for January 20, 2021. Frames (a) and (b) show the synthetic waveforms for the two sets of detonations. The purple trace corresponds to the one shown in Figure 3. Frames (c) and (d) show the correlation coefficient with respect to the first trace from each set, and frames (e) and (f) show the computed time delay. The red crosses represent nonphysical data points (e.g., time delay of 10 s), and they are placed in the middle of the vertical axis. Frames (g) and (h) show an example of the observed signal at Eastern Oklahoma College from the middle of each set (light green traces in frames (a) and (b)). The detonation sequence (as recorded at MCA) starts at 17:00:46 UTC and ends at 17:19:25 UTC.

Figure 3b shows that all the energy that arrives at EOC is trapped in the low-altitude waveguide, refracting from altitudes between 0.5 and 2 km. Such a low-altitude waveguide leads to a complex multipath propagation. Figure 3d shows the broadband simulations results. The atmospheric models predict two distinct behaviors. First, the amplitude of the signals increases in time. Second, the signals' arrival time decreases over time, that is, the waves propagate faster.

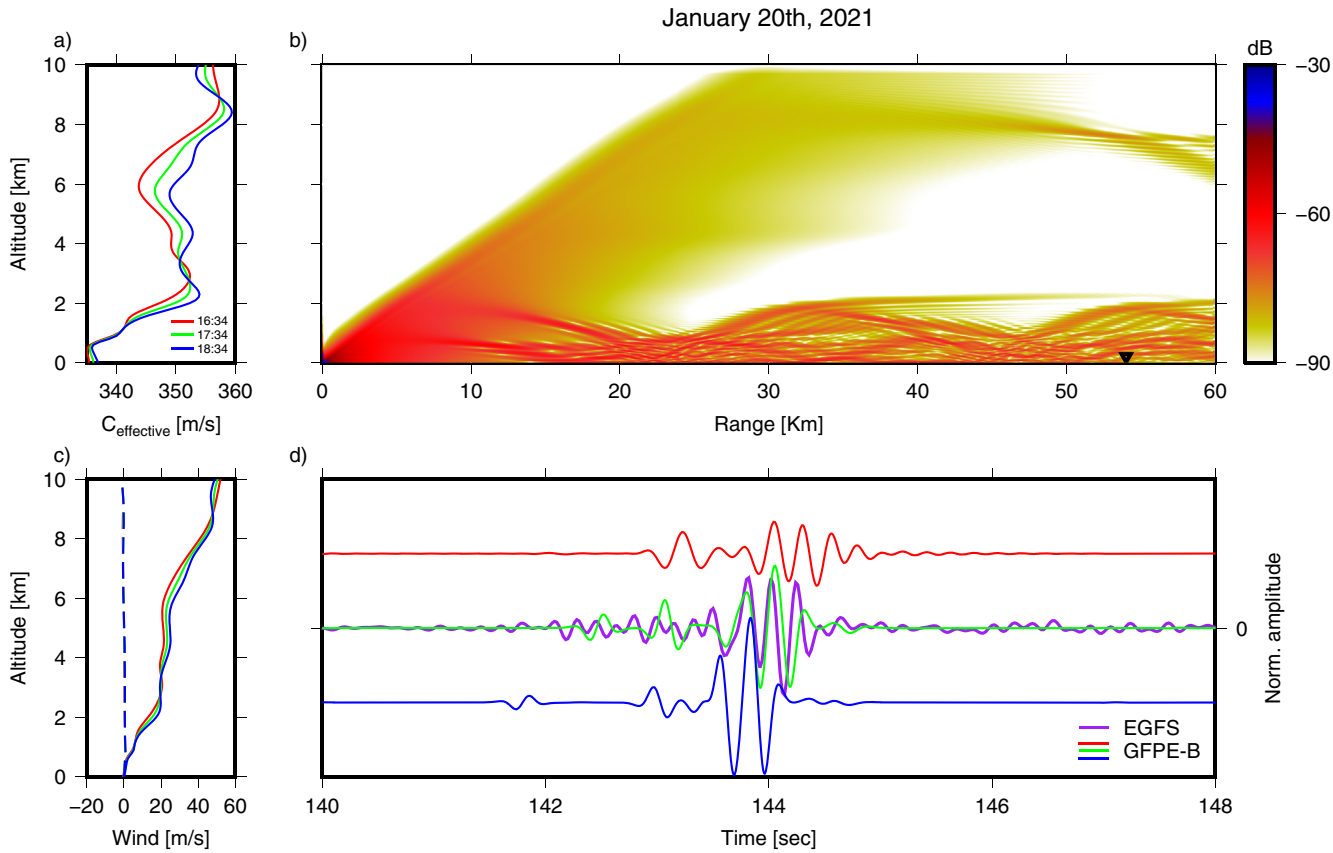

Figure 3. Green's function Parabolic Equation (GFPE) narrowband and broadband simulations for January 20, 2021. Frame (a) shows the effective speed of sound. Frame (c) shows the along-track (solid), and cross-track (dashed) wind profiles. The red, green, and blue colors correspond to 16:34, 17:34, and 18:34 UTC in both frames. Frame (b) shows the narrowband simulation results for a 10 Hz source at 17:43 UTC, and the black triangle marks the location of the EOC array. Frame (d) shows a comparison between the GFPE-B (red, green, and blue) and empirical Green's functions based synthetics (EGFS) waveforms (purple). The colored waveforms correspond to the colored effective speed of sound. The correlation coefficient between the green and purple waveforms is 0.036, and the purple waveform corresponds to the purple trace in Figure 2. All traces are normalized.

Figure 3d also compares between an EGFS and the GFPE-B (purple and green traces). The atmospheric model predicts three phases; two low-amplitude phases followed by a high amplitude one. It can be seen that the atmospheric model predicts the general structure of the primary phase. From the EGFS, it is not clear if the preceding two phases are observed or not. If the low-amplitude disturbances on the second set (Figure 2b) are their corresponding phases, then the atmospheric model overestimates their amplitudes and propagation time.

4.2. February 2, 2021

On February 2, 2021, there was one set of shots from area 2. Figure 4a shows the waveform's evolution in time. It can be seen that the signal starts with a clear Ricker-like waveform and slowly deforms over time. The transition to a more complex waveform indicates the change in the propagation conditions. Since the first trace is "noisy," the last trace is used as a reference for the cross correlation. Also here, the correlation coefficient varies within tens of seconds. Additionally, the steady change of time delays (Figure 4c) is similar to the one observed in Figure 2d. It is important to keep in mind that the reason for the opposite behavior of the correlation coefficient and time delay in Figure 4 compared to Figure 2 is due to the use of the last trace as a reference and not the first one.

As in Section 4.1, a low-altitude waveguide traps the energy in the first kilometer of the atmosphere (Figure 5b). In addition, the atmospheric models predict a decrease in arrival time (Figure 5d) Comparing the EGFS to the GFPE-B shows a good agreement (Figure 5d). However, the perturbations before and after the primary signal are not adequately captured. These minor discrepancies can be attributed to small-scale atmospheric structures

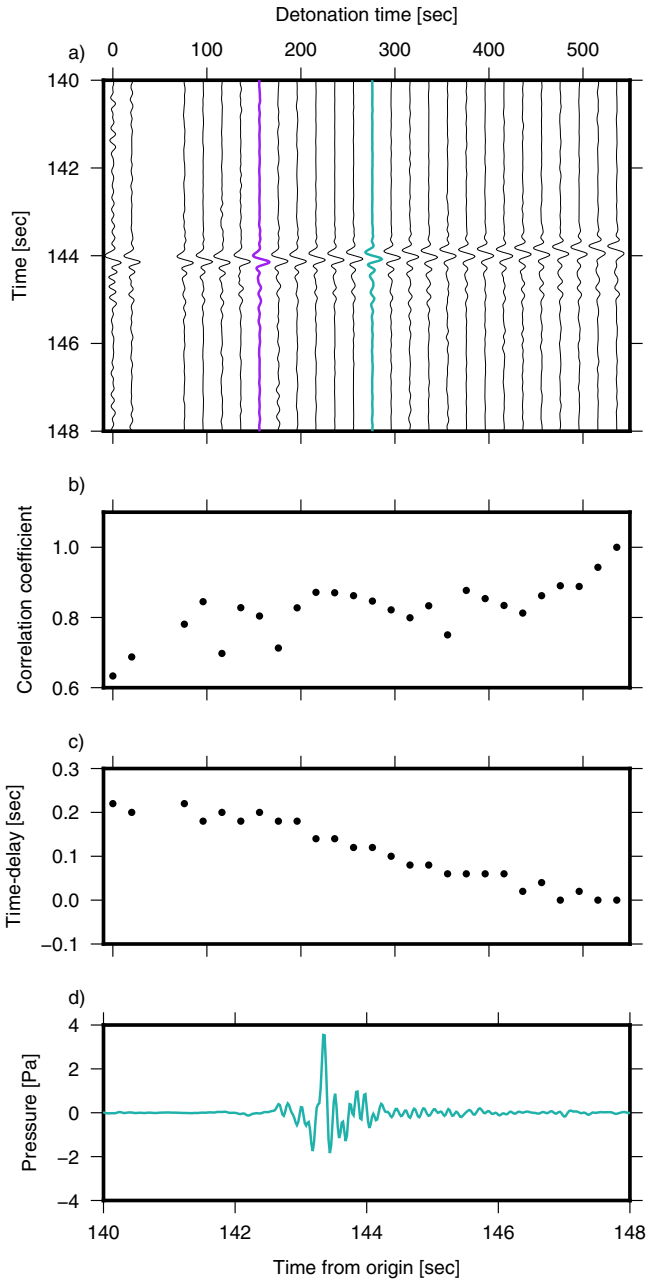

Figure 4. Same as Figure 2 for February 2, 2021. Since the first trace is "noisy," the last trace is used as a reference for the correlation coefficient. The detonation sequence (as recorded at MCA) starts at 17:01:01 UTC and ends at 17:10:00 UTC.

that the atmospheric model does not resolve and/or local noise at EOC that contaminates the signal. In addition, the EGFS is slightly dispersed compared to the GFPE-B signal.

4.3. February 5, 2021

On February 5, 2021, the signals start with two distinct phases at 143 and 145 s (Figure 6a) During the first set, the amplitude of the first phase increases while the waveforms of the second phase change. One can notice the two-second difference in the arrival times between the first and second sets. As in Section 4.1, it is attributed to the distance between areas 1 and 2. However, in this case, the first set comes from area 2. On the second set (Figure 6b), the amplitude of the first phase continues to increase while the waveforms of the second phase keep changing. As in Sections 4.1 and 4.2, the correlation coefficients decrease in time, and the time delays have distinct patterns. The steady increase of time delays in Figure 6e is attributed to the linear geometry of area 2, and the periodic-like behavior in Figure 6f is attributed to the shape of area 1.

The atmospheric models predict two phases arriving at EOC (Figure 7d). These two phases are related to two different propagation paths. Figure 7b shows that most of the energy that arrives at EOC refracts from altitudes between 3 and 5 km. This propagation path corresponds to the simulated phase around 144–145 s in Figure 7b, which is related to the second observed phase at the EGFS (Figures 6a and 6b). It can be seen that some of the energy is also trapped within the first kilometer of the atmosphere. This low-altitude waveguide is formed due to stronger along-track winds (Figure 7c); it corresponds to the first simulated phase that exists earlier (16:34 UTC) and is predicted to decay over time. Additionally, this phase corresponds to the first observed phase in Figures 6a and 6b. A comparison between the EGFS and GFPE-B signals in Figure 7d shows that the atmospheric models correctly predicted the second phase. However, the amplitude of the first phase (compared to the second one) is underestimated. In addition, while the atmospheric models predict the disappearance of the first phase, the observations show the opposite. Furthermore, the waves are predicted to propagate faster over time.

5. Discussion

The presented results show that infrasonic waveforms and propagation times can change over timescales ranging between tens of seconds to minutes. This section summarizes the broad trends and provides additional comparative analyses of the observations. Finally, we provide a qualitative assessment of what the observations imply about unresolved changes in the atmospheric state.

On January 20, 2021, signals from the first set start with two distinct phases where the second arrival is the prominent one. Over 10 min, the waveforms significantly change, and by the time of the second set, there is only one noticeable phase. A comparison with the simulated signal (Figure 3d) shows a good agreement with the highest-amplitude phase. However, it is not clear whether the preceding predicted phases exist in the observations or not. If one interprets the wiggles between 142 and 144 s as these phases, then the atmospheric model overestimates their amplitudes, and they arrive 0.3 s later than observed.

Signals from February 5, 2021, also showed significant changes in their waveforms. The most noticeable change is the increase in the amplitude of the first arrival. This phase is associated with a slight increase in the effective speed of sound at an altitude of 1 km, which leads to a near-ground horizontal propagation path (Figure 7). The

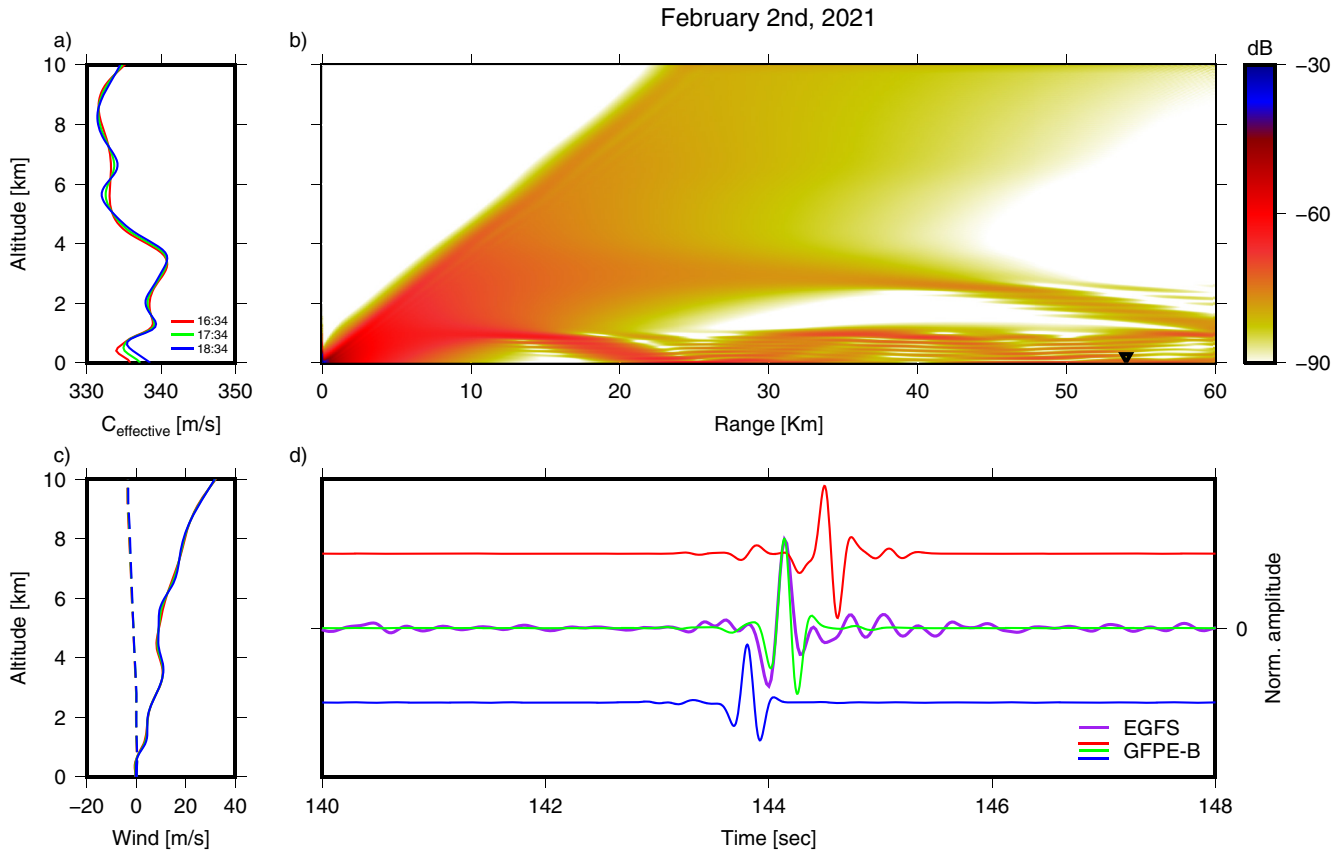

Figure 5. Same as Figure 3 for February 2, 2021. The correlation coefficient between the green and purple waveforms is 0.029.

estimated lower amplitude of this phase is probably due to lower wind estimation by the atmospheric model that leads to less trapped energy. Therefore, increasing wind at this altitude can explain the increase in amplitudes of the first arrival. Such an increase allows trapping more acoustic energy and leads to higher amplitudes of the associated signals. Interestingly, the atmospheric models predicted such a waveguide (and the phase) 1 hr earlier, as well as its weakening over time (Figure 7), which is opposite of the observations.

Following the variations of the signals' amplitudes, Figure 8 shows the change in TL of the EGFS, where a different pattern is apparent for each day. As mentioned in Section 3.2, by using the EGFS, source effects have been removed, and any variation in them is attributed to variations in the atmosphere. Generally, an increase in TL suggests that the atmospheric waveguides trap more acoustic energy and vice versa. On January 20, 2021, TL values consist of an increasing trend with some fluctuations. The increase in TL values is in line with the numerical simulations that predict an increase in the signal's amplitude due to the strengthening of the waveguide over time (Figure 3) An increase following a decrease in TL values is observed during the only set on February 2, 2021, and on February 5, 2021, a periodic pattern is observed; the predicted variations of the effective speed of sound profiles in Figures 3, 5, and 7 cannot explain such fluctuation. In order to evaluate their periods, the Lomb-Scargle Periodogram is used. This method evaluates the spectral components of unevenly sampled data (Collaboration et al., 2018; Scargle et al., 1982). Results show that the characteristic periods range between 100 and 160 s for all days. The link between these observed changes and propagation conditions raises the question of whether a particular atmospheric phenomenon can explain them.

To the best of our knowledge, this question has not been addressed before. However, the correlation between ambient pressure perturbation and atmospheric phenomena has been shown in previous studies. Posmentier (1974) relates pressure fluctuations in a frequency range of 1–16 Hz, measured on the ground, to the compressional properties of clear air turbulence. Cuxart et al. (2016) show a correlation between infrasound energy (0.01–15 Hz) to turbulent kinetic energy (TKE) and the standard deviation of the vertical velocity (used as a measure

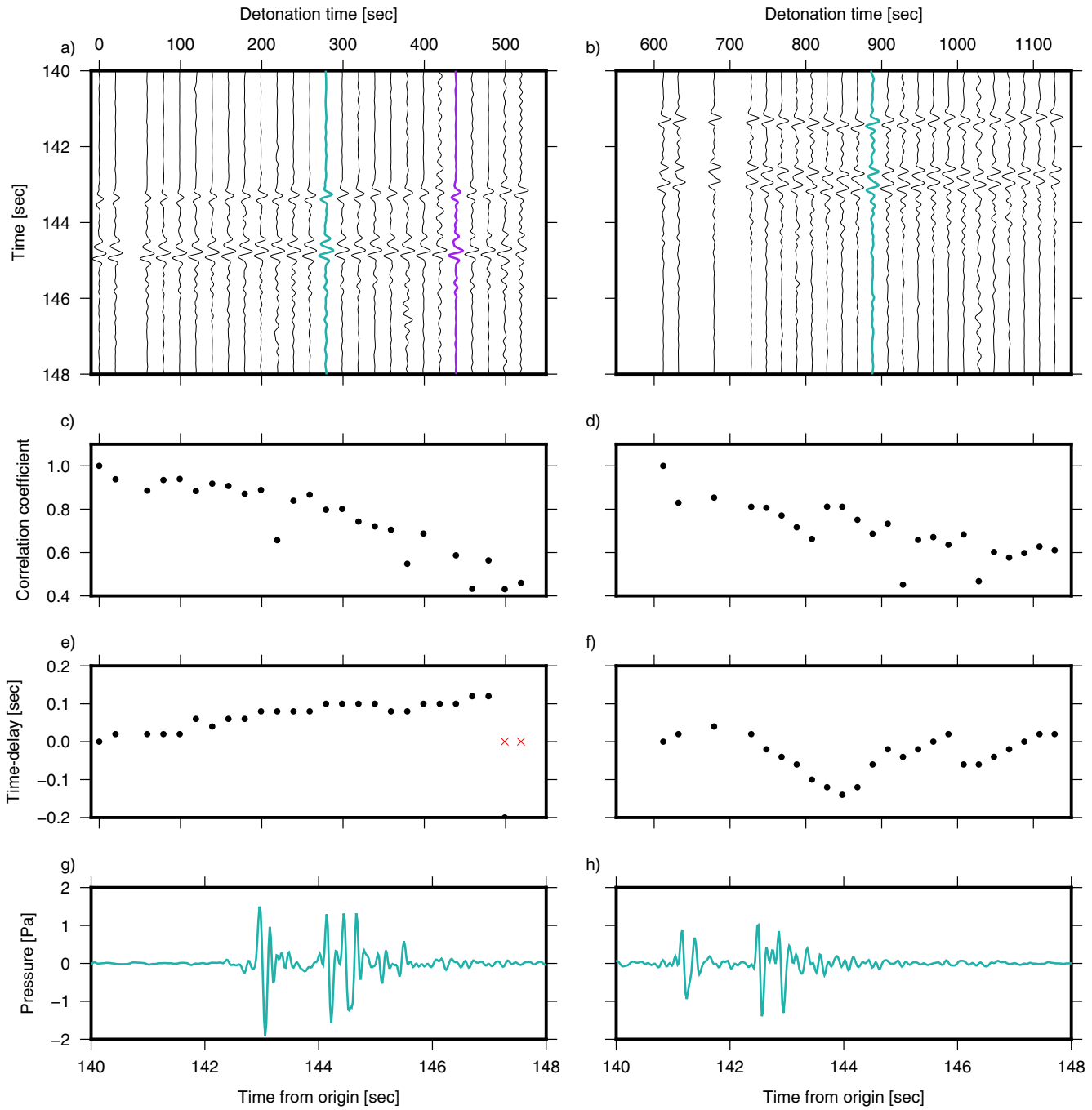

Figure 6. Same as Figure 2 for February 5, 2021. The detonation sequence (as recorded at MCA) starts at 17:01:24 UTC and ends at 17:20:12 UTC.

for turbulence sources above the surface layer). In addition, the authors state that larger turbulence causes lower-frequency pressure perturbations with characteristic frequencies of 0.001 Hz (acoustic-gravity waves). Other studies used microbarometer arrays to detect low-frequency (1–10 cycles per hour) gravity waves that originated by wind perturbations in the tropospheric jet stream (Herron et al., 1969; Herron & Tolstoy, 1969; Tolstoy & Herron, 1969). Besides the low-frequency pressure perturbations, gravity waves perturb the wind field (Tolstoy & Herron, 1969). Therefore, the wind speed will fluctuate due to the passage of gravity waves. Such fluctuations affects infrasound travel time, waveforms, and phases (Chunchuzov & Kulichkov, 2019; Drob et al., 2013). A typical Brunt-Väisälä period in the atmosphere is about 340 s. This value sets a lower limit for the gravity waves periods. Therefore, the observed fluctuations in Figure 8 are not directly related to gravity waves. Usually,

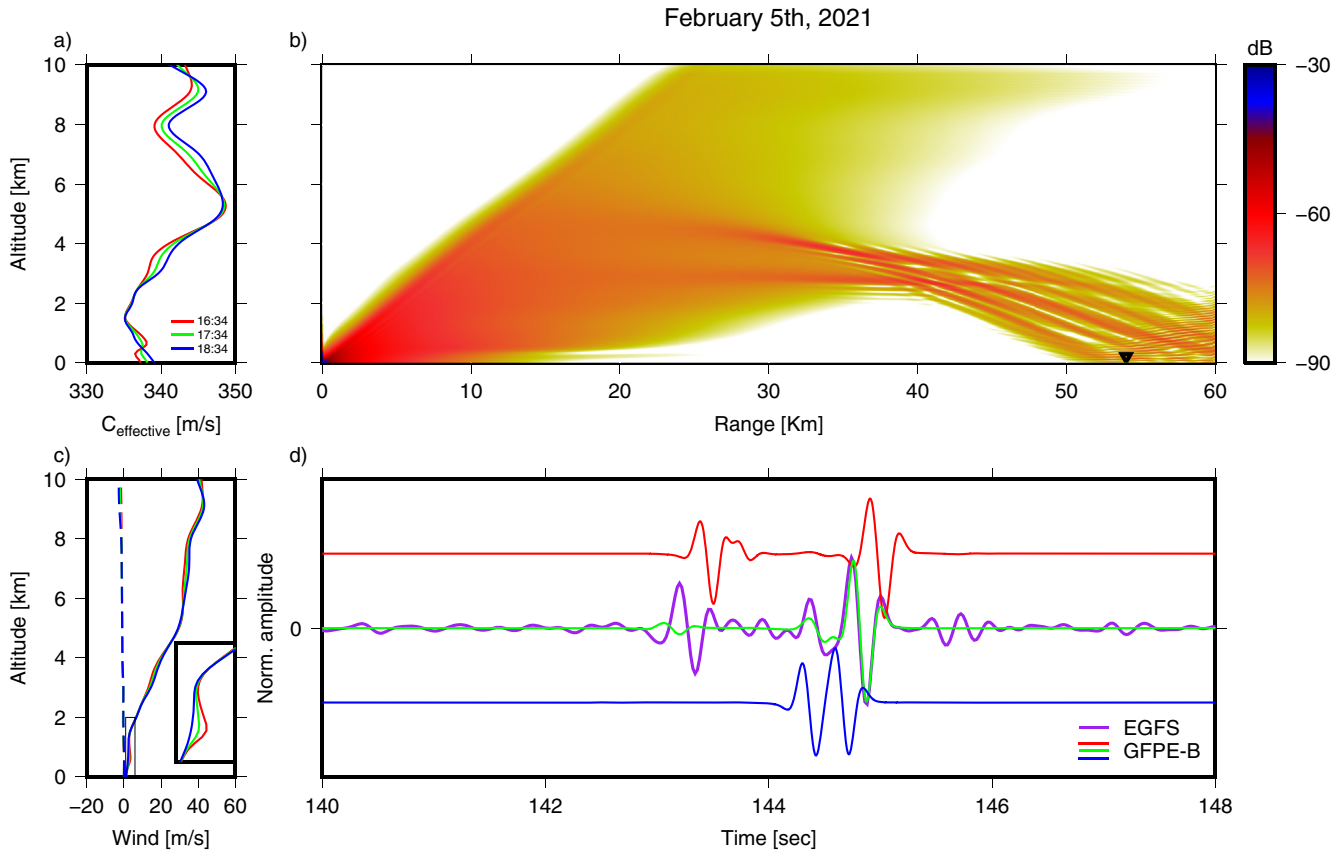

Figure 7. Same as Figure 3 for February 5, 2021. The correlation coefficient between the green and purple waveforms is 0.046.

variations in such periods correspond to phenomena with length scales of hundreds of meters to tens of kilometers (Drob, 2019; Stull, 2017). Moreover, the sensitivity of the infrasonic waves to various small-scale atmospheric structures depends on the frequency spectrum. Therefore, using higher frequencies (if possible) may lead to observed variations with shorter periods than the ones observed in this study; such shorter periods will also be linked to phenomena with shorter length scales. Following the mentioned studies that linked observed pressure perturbations to specific atmospheric phenomena, we can also ask: is there a specific phenomenon that explains fluctuations in such periods? Furthermore, if there is one (or more), can we use such observations to characterize it? These questions are promising topics for future work.

In addition to the variability in the signals' amplitudes, the results also show variations in arrival times. As mentioned in Section 4, these variations are partly explained by the shapes of areas 1 and 2. Since area two is linear, it is simple to estimate the contribution of its dimension to the observed time delays. Therefore, the following analysis focuses solely on area 2.

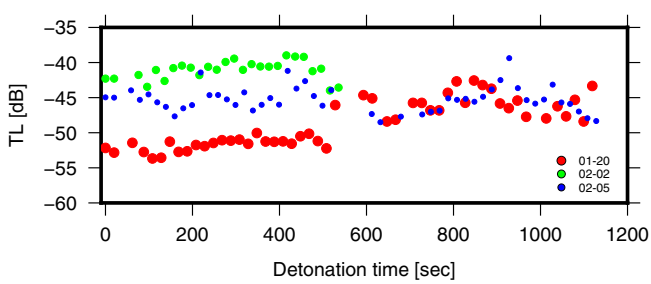

Figure 8. Computed transmission loss (TL) values for all empirical Green's functions.

Figure 9 shows the computed time delays of the shots from area 2 for all 3 days. The dashed black line represents the expected time delay due to the linear shape of the area based on celerity of 330 m/s; the maximum expected time delay is 0.113 s. A maximum time delay of 0.107 s is obtained by changing the value to 350 m/s (dotted line). Hence, the shape of the area explains only part of the observed time delays.

Assuming lower speed-of-sound values to explain the excess time delays lead to nonphysical values. Therefore, the surplus time delay can be attributed to increased celerity, that is, the effective sound speed aloft. It means that the waves propagate faster over time, and the arrival time decreases. Such a decrease in the arrival time is predicted in all 3 days (Figures 3, 5, and 7d).

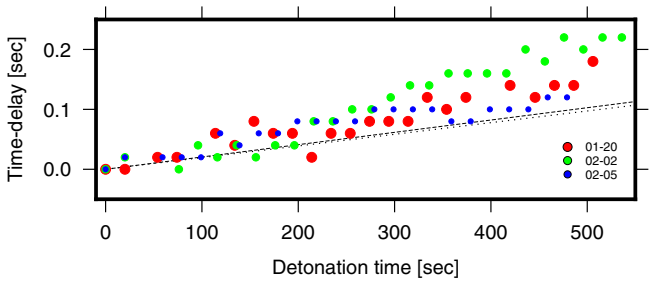

Figure 9. Time delays for the 3 days from Area 2. The dashed black line represents the expected time delay due to the linear shape of Area 2, based on celerity of 330 m/s. The dotted line represents the expected time delay based on celerity of 350 m/s. Results from Figure 4c are flipped to match the increasing trend.

Furthermore, on January 20 and February 5, 2021, the models predicted a similar delay time, and they underestimated it on February 2, 2021. These results show that also travel times are sensitive to short temporal atmospheric variations.

It has been shown that infrasound decorrelation time is in the order of tens of seconds to minutes. While the signal phases, and amplitude affect (de)correlation, it is shown that travel time changes over similar timescales. These results mean that if one were to use infrasound waveform information to probe the atmosphere, the observed atmospheric temporal variability would be within the same temporal scales.

6. Conclusions

The propagation of infrasound in the atmosphere is affected by the spatial and temporal variations of temperature and wind. This study investigates the timescales and nature at which atmospheric variability affects infrasound signals. Specifically, we test the temporal variability of infrasound properties such as back azimuth, apparent velocity, waveforms, propagation time, and energy. The study is based on the recording of a repetitive infrasound source and its corresponding signals that propagate through the atmospheric boundary layer and lower atmosphere (up to 5 km).

Array processing results show small apparent velocity and back azimuth values variability. However, the relatively small array aperture leads to a significant variance of the array resolution. Therefore, these values were not used for further analysis. Nevertheless, based on the arrays' best beams, the EGFS show that infrasound waveforms, propagation time, and energy vary on timescales of tens of seconds.

The EGFS show a significant waveform transformation that leads to signals' decorrelation within tens of seconds to minutes. The observed time delay variations are partly related to the distances between the detonation pits. The sensitivity of the propagation time to variations of meters in the source location is essential for detecting and locating infrasound sources and of importance for the Comprehensive Nuclear-Test-Ban Treaty Organisation operations. In addition, the excess time delay (that is not explained by the layout of areas 1 and 2) suggests that the effective sound speed increases due to an average increase in temperature and wind. This observation is captured by the atmospheric models that predict a similar decrease in propagation time.

Observed fluctuations in the signal's energy suggest that the atmospheric waveguide's ability to trap acoustic energy changes over time. Particularly, since winds facilitate the low-tropospheric waveguide, changes in the signals' energy indicate wind changes. Spectral analysis shows that the observed fluctuations have periods ranging from 100 to 160 s. However, pointing out the exact mechanism that generates such fluctuations remains an open question.

To conclude, all the observed variations in the signals' phases, waveforms, travel times, and energy are related to variations in temperature and wind. Therefore, this study highlights the potential of high temporal resolution infrasound-based atmospheric sounding. Moreover, variations in wind and temperature are related to other dynamic processes (e.g., radiation, gravity waves, and turbulence). The research question regarding relating specific phenomena and their magnitude to such observations (Section 1) was not answered in this study and, therefore, should be the focus of future studies. In addition, other experimental setups should be considered. For example, deploying multiple arrays to cover a high azimuthal range will allow us to quantify winds better. Also, deploying line arrays can be used to study the atmosphere's spatial variability. Finally, an ongoing second phase of this study focuses on short temporal stratospheric variability.

Appendix A: EOC Beamforming Example

Figure A1 shows the EOC's array configuration and response. The array response is centered at an azimuth of 257° and an apparent velocity of 340 m/s. These values correspond to the azimuth toward McAAP detonation sites and a typical detected apparent velocity. Figure A1c shows the array response for a given apparent velocity as a function of azimuth. The relatively small array aperture leads to a high variance in the back azimuth resolution.

10.1029/2021EA002036

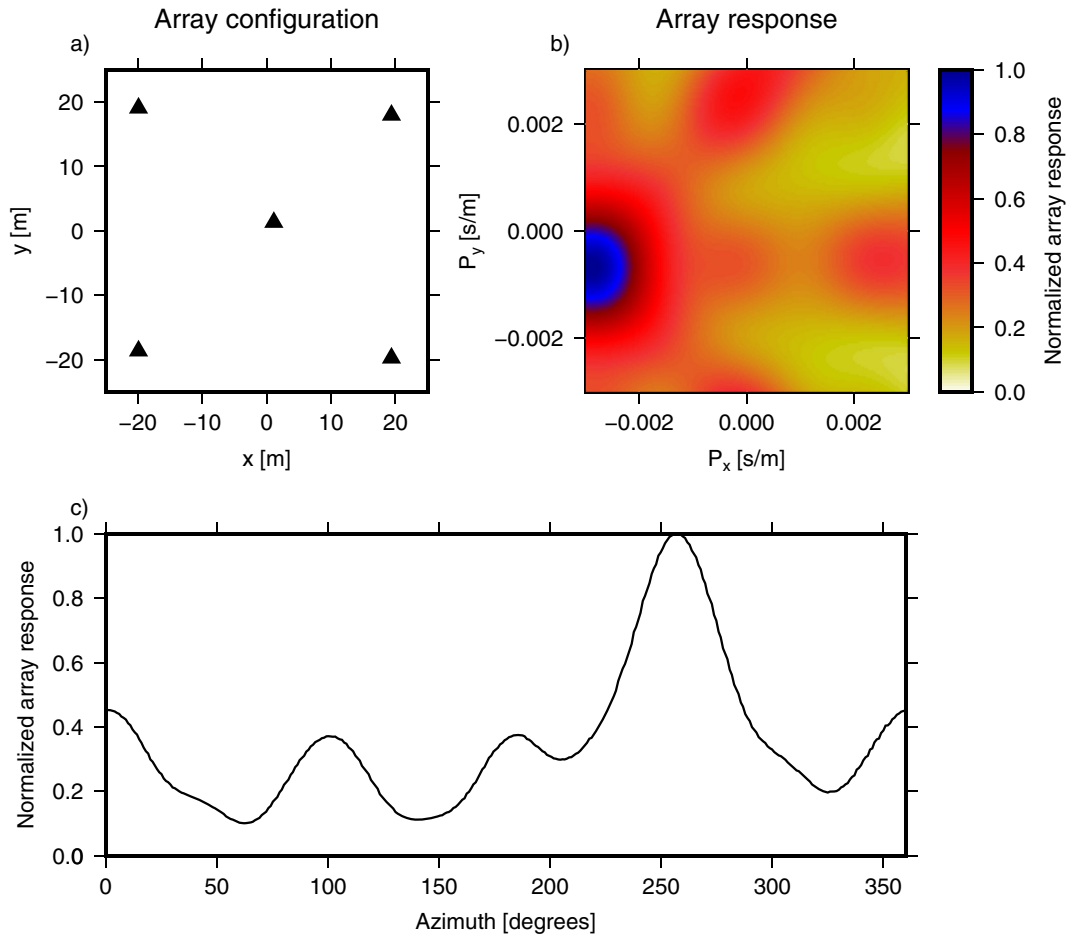

Figure A1. EOC roof array response. Frame (a) shows the array configuration. Frame (b) shows the array response centered at an azimuth of 257° and an apparent velocity of 340 m/s. Frame (c) shows the array response for an apparent velocity of 340 m/s.

Figure A2 shows an example of beamforming results from January 20, 2021. Data are bandpass-filtered between 1 and 10 Hz, and a 15-s sliding window is used with an overlap of 95%. The apparent velocity and back azimuth frames show variations in the detected values. However, due to the high variance of the array resolution (Figure A1) these observations are not used to study the atmosphere's variability.

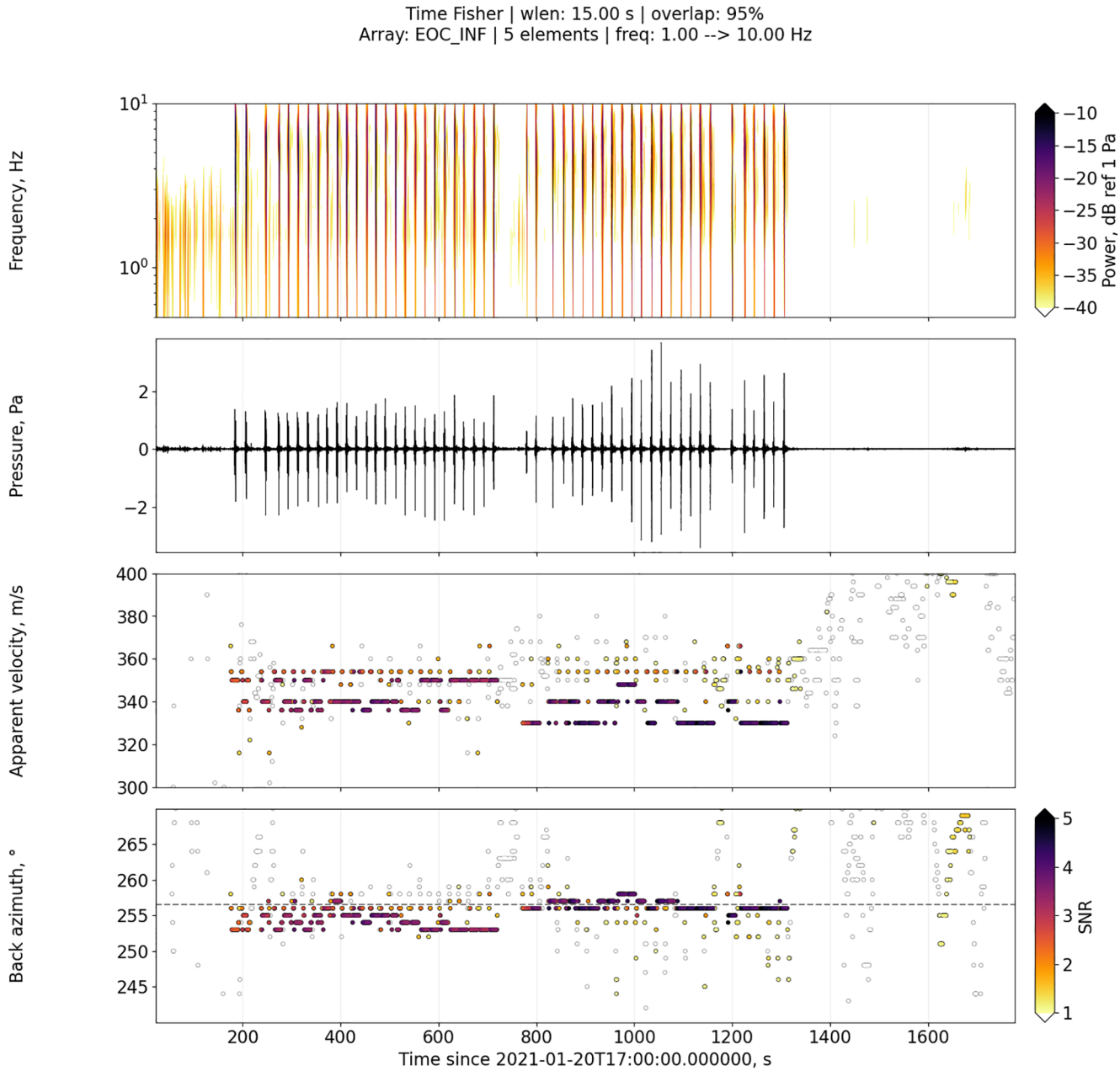

Figure A2. Beamforming results for January 20, 2021. Frames from top to bottom show: the spectrogram, best beam, apparent velocity, and back azimuth. The dashed line points toward the midpoint between areas 1 and 2.

Appendix B: McAAP Waveforms Comparison

Due to access problems, the MCA array was placed outside of McAAP. Four months later, we were granted permission to enter McAAP and deploy sensors closer to the detonation site (4 km). In addition, we deployed sensors at the MCA location (7 km). Figure B1 shows four waveform examples from July 8 and 9, 2021. The data are bandpass-filtered between 1 and 10 Hz and scaled. One can see that besides the low-amplitude coda, the waveforms perfectly match.

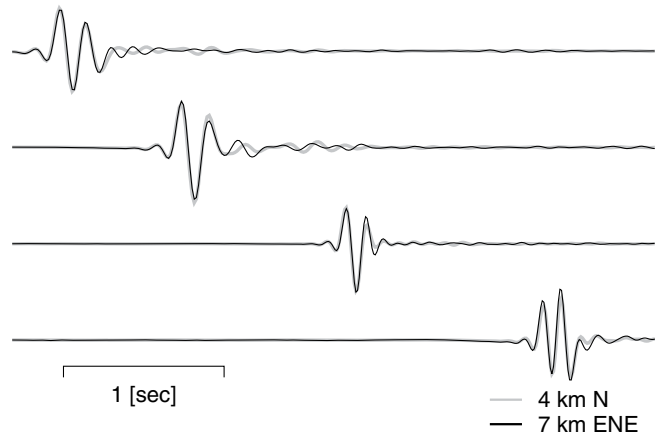

Figure B1. Four examples of waveform comparison from two locations at McAAP. The first is 4 km north (N) to areas 1 and 2, and the second is 7 km east-north-east (ENE) from the areas. From top to bottom, the first two signals are from July 8, 2021, 267 and 287 s after 16:00 UTC. The two bottom signals are from July 9, 2021, 1,038 and 1,139 s after 16:00 UTC. The timing of the signals is stated at the northern location and a reduced time axis is used to align them.

Data Availability Statement

Data are available via IRIS (https://doi.org/10.7914/SN/3B_2021) under the network 3B, and stations EOC and MCA.

Acknowledgments
We would like to thank Gideon Rogers and Leah Thomas from McAlester Army Ammunition Plant, and Patricia Ratliff from Eastern Oklahoma State College for supporting our measurement campaign. Also, we would like to thank Claus Hetzer for maintaining the NCPA server (http://130.74.32.249/), and Chris Hayward and Art Endress for technical support. Finally, we would like to thank Sven Peter Näsholm and the anonymous reviewers for their comments.

References

Amezcua, J., & Barton, Z. (2021). Assimilating atmospheric infrasound data to constrain atmospheric winds in a two-dimensional grid. *Quarterly Journal of the Royal Meteorological Society*, *147*, 3530–3554. https://doi.org/10.1002/QJ.4141

Amezcua, J., Näsholm, S. P., Blixt, E. M., & Charlton-Perez, A. J. (2020). Assimilation of atmospheric infrasound data to constrain tropospheric and stratospheric winds. *Quarterly Journal of the Royal Meteorological Society*, *146*(731), 2634–2653. https://doi.org/10.1002/qj.3809

Anderson, J. F., Johnson, J. B., Bowman, D. C., & Ronan, T. J. (2018). The Gem infrasound logger and Custom-Built Instrumentation. *Seismological Research Letters*, *89*(1), 153–164. https://doi.org/10.1785/0220170067

Anderson, J. F., Johnson, J. B., Steele, A. L., Ruiz, M. C., & Brand, B. D. (2018). Diverse eruptive activity revealed by acoustic and electromagnetic observations of the 14 July 2013 Intense Vulcanian eruption of Tungurahua volcano, Ecuador. *Geophysical Research Letters*, *45*, 2976–2985. https://doi.org/10.1002/2017GL076419

Applbaum, D., Averbuch, G., Price, C., Yair, Y., & Ben-Horin, Y. (2020). Infrasound observations of sprites associated with winter thunderstorms in the eastern mediterranean. *Atmospheric Research*, *235*, 104770. https://doi.org/10.1016/j.atmosres.2019.104770

Arrowsmith, S. J. (2018). False alarms and the IMS infrasound network: Understanding the factors influencing the creation of false events. *Geophysical Journal International*, *215*(2), 1322–1337. https://doi.org/10.1093/GJI/GGY350

Arrowsmith, S. J., Johnson, J. B., Drob, D. P., & Hedlin, M. A. (2010). The seismoacoustic wavefield: A new paradigm in studying geophysical phenomena. *Reviews of Geophysics*, *48*, 1–23. https://doi.org/10.1029/2010RG000335

Arrowsmith, S. J., Park, J., Che, I.-Y., Stump, B., & Averbuch, G. (2021). Event location with sparse data: When probabilistic Global Search is important. *Seismological Research Letters*, *92*(2A), 976–985. https://doi.org/10.1785/0220200292

Assink, J. D., Averbuch, G., Shani-Kadmiel, S., Smets, P., & Evers, L. (2018). A seismo-acoustic analysis of the 2017 north Korean nuclear test. *Seismological Research Letters*, *89*(6), 2025–2033. https://doi.org/10.1785/0220180137

Assink, J. D., Averbuch, G., Smets, P. S., & Evers, L. G. (2016). On the infrasound detected from the 2013 and 2016 DPRK's underground nuclear tests. *Geophysical Research Letters*, *43*, 3526–3533. https://doi.org/10.1002/2016GL068497

Assink, J. D., Waxler, R., & Drob, D. (2012). On the sensitivity of infrasonic traveltimes in the equatorial region to the atmospheric tides. *Journal of Geophysical Research: Atmospheres*, *117*, D01110. https://doi.org/10.1029/2011JD016107

Assink, J. D., Waxler, R., Frazier, W. G., & Lonzaga, J. (2013). The estimation of upper atmospheric wind model updates from infrasound data. *Journal of Geophysical Research: Atmospheres*, *118*, 10707–10710. https://doi.org/10.1002/jgrd.50833

Averbuch, G. (2021). The spectrogram, method of reassignment, and frequency-domain beamforming. *Journal of the Acoustical Society of America*, *149*(2), 747–757. https://doi.org/10.1121/10.0003384

Averbuch, G., Assink, J. D., Smets, P. S. M., & Evers, L. G. (2018). Extracting low signal-to-noise ratio events with the Hough transform from sparse array data. *Geophysics*, *83*(3), WC43–WC51. https://doi.org/10.1190/geo2017-0490.1

Averbuch, G., Ben-Horin, Y., Smets, P. S. M., & Evers, L. G. (2019). The mount Meron infrasound array: An infrasound array without a noise reduction system. *Geophysical Journal International*, *219*, 1109–1117. https://doi.org/10.1093/gji/ggz350

Blixt, E. M., Näsholm, S. P., Gibbons, S. J., Evers, L. G., Charlton-Perez, A. J., Orsolini, Y. J., & Kværna, T. (2019). Estimating tropospheric and stratospheric winds using infrasound from explosions. *Journal of the Acoustical Society of America*, *146*(2), 973–982. https://doi.org/10.1121/1.5120183

Brekhovskikh, L., Goncharov, V., Kurtepov, V., & Ka, N. (1973). Radiation of infrasound into atmosphere by surface-waves in ocean. *Izvestiya Akademii Nauk SSSR Fizika Atmosfery i Okeana*, *9*(9), 899–907.

Butler, A. H., Sjoberg, J. P., Seidel, D. J., & Rosenlof, K. H. (2017). A sudden stratospheric warming compendium. *Earth System Science Data*, *9*(1), 63–76. https://doi.org/10.5194/ESSD-9-63-2017

Carmichael, J. D., Thiel, A. D., Blom, P. S., Walter, J. I., Dugick, F. K. D., Arrowsmith, S. J., & Carr, C. G. (2021). Persistent, "Mysterious" seismoacoustic signals reported in Oklahoma state during 2019. *Bulletin of the Seismological Society of America*. https://doi.org/10.1785/0120210145

Chunchuzov, I., & Kulichkov, S. (2019). Internal gravity wave perturbations and their impacts on infrasound propagation in the atmosphere. In *Infrasound monitoring for atmospheric studies: Challenges in middle atmosphere dynamics and Societal Benefits* (2nd ed., pp. 551–590). https://doi.org/10.1007/978-3-319-75140-5_16

Collaboration, A., Price-Whelan, A. M., Sipőcz, B. M., Günther, H. M., Lim, P. L., Crawford, S. M., et al. (2018). The Astropy Project: Building an open-science Project and Status of the v2.0 Core Package. *The Astronomical Journal*, *156*(3), 123. https://doi.org/10.3847/1538-3881/AABC4F

Collins, M. D., & Siegmann, W. L. (2019). *Parabolic wave equations with applications* (1st ed.,pp. 1–135). Springer. https://doi.org/10.1007/978-1-4939-9934-7

Cuxart, J., Tatrai, D., Weidinger, T., Kircsi, A., Józsa, J., & Kiss, M. (2016). *Infrasound as a detector of local and remote turbulence* (Vol. 159, No. 2). Dordrecht, The Netherlands: Springer. https://doi.org/10.1007/s10546-015-0100-2

Dahlman, O., Mykkeltveit, P., & Haak, H. (2009). The treaty. In *Nuclear test ban* (pp. 83–98). Dordrecht, The Netherlands: Springer. https://doi.org/10.1007/978-1-4020-6885-0_4

De Carlo, M., Hupe, P., Le Pichon, A., Ceranna, L., & Ardhuin, F. (2021). *Global microbarom patterns: A first confirmation of the theory for source and propagation* (Vol. 48, No. 3). Blackwell Publishing Ltd. https://doi.org/10.1029/2020GL090163

den Ouden, O. F. C., Assink, J. D., Smets, P. S. M., Shani-Kadmiel, S., Averbuch, G., & Evers, L. G. (2020). CLEAN beamforming for the enhanced detection of multiple infrasonic sources. *Geophysical Journal International*, *221*(1), 305–317. https://doi.org/10.1093/gji/ggaa010

Desanto, J. (1992). *Scalar wave theory. Green's functions and applications* (1st ed.). Berlin: Springer-Verlag. https://doi.org/10.1007/978-3-642-84738-7

Diamond, M. (1964). Cross wind effect on sound propagation. *Journal of Applied Meteorology*, *3*(2), 208–210. https://doi.org/10.1175/1520-0450(1964)003<0208:CWEOSP>2.0.CO;2

Donn, W. L., & Posmentier, E. S. (1964). Ground-coupled air waves from the Great Alaskan earthquake. *Journal of Geophysical Research*, *69*(24), 5357–5361. https://doi.org/10.1029/JZ069i024p05357

Drob, D. P. (2019). Meteorology, climatology, and upper atmospheric composition for infrasound propagation modeling. In *Infrasound monitoring for atmospheric studies: Challenges in middle atmosphere dynamics and Societal Benefits* (2nd ed., pp. 485–508). https://doi.org/10.1007/978-3-319-75140-5_14

Drob, D. P., Broutman, D., Hedlin, M. A., Winslow, N. W., & Gibson, R. G. (2013). A method for specifying atmospheric gravity wavefields for long-range infrasound propagation calculations. *Journal of Geophysical Research: Atmospheres*, *118*, 3933–3943. https://doi.org/10.1029/2012JD018077

Drob, D. P., Emmert, J. T., Meriwether, J. W., Makela, J. J., Doornbos, E., Conde, M., et al., (2015). An update to the Horizontal Wind Model (HWM): The quiet time thermosphere. *Earth and Space Science*, *2*(7), 301–319. https://doi.org/10.1002/2014EA000089

Drob, D. P., Meier, R. R., Picone, J. M., & Garcés, M. M. (2009). Inversion of infrasound signals for passive atmospheric remote sensing. In A. Le Pichon, E. Blanc, & A. Hauchecorne (Eds.), *Infrasound monitoring for atmospheric studies* (pp. 701–731). Dordrecht, The Netherlands: Springer. https://doi.org/10.1007/978-1-4020-9508-5_24

Drob, D. P., Picone, J. M., & Garcés, M. (2003). Global morphology of infrasound propagation. *Journal of Geophysical Research*, *108*(D21), 4680. https://doi.org/10.1029/2002JD003307

Evers, L. G., Assink, J. D., & Smets, P. S. M. (2018). Infrasound from the 2009 and 2017 DPRK rocket launches. *Geophysical Journal International*, *213*(3), 1785–1791. https://doi.org/10.1093/gji/ggy092

Evers, L. G., Brown, D., Heaney, K. D., Assink, J. D., Smets, P. S., & Snellen, M. (2014). Evanescent wave coupling in a geophysical system: Airborne acoustic signals from the Mw 8.1 Macquarie Ridge earthquake. *Geophysical Research Letters*, *41*, 1644–1650. https://doi.org/10.1002/2013GL058801

Evers, L. G., & Haak, H. W. (2005). The detectability of infrasound in The Netherlands from the Italian volcano Mt. Etna. *Journal of Atmospheric and Solar-Terrestrial Physics*, *67*(3), 259–268. https://doi.org/10.1016/j.jastp.2004.09.002

Evers, L. G., & Haak, H. W. (2010). The characteristics of infrasound, its propagation and some early history. In *Infrasound monitoring for atmospheric studies* (pp. 3–27). Dordrecht, The Netherlands: Springer. https://doi.org/10.1007/978-1-4020-9508-5_1

Fee, D., & Garcés, M. (2007). Infrasonic tremor in the diffraction zone. *Geophysical Research Letters*, *34*, L16826. https://doi.org/10.1029/2007GL030616

Fee, D., Waxler, R., Assink, J., Gitterman, Y., Given, J., Coyne, J., & Grenard, P. (2013). Overview of the 2009 and 2011 Sayarim infrasound Calibration Experiments. *Journal of Geophysical Research: Atmospheres*, *118*, 6122–6143. https://doi.org/10.1002/jgrd.50398

Feit, M. D., & Fleck, J. A. (1978). Light propagation in graded-index optical fibers. *Applied Optics*, *17*(24), 3990. https://doi.org/10.1364/ao.17.003990

Fricke, J., Evers, L., Smets, P., Wapenaar, K., & Simons, D. (2014). Infrasonic interferometry applied to microbaroms observed at the large aperture infrasound array in The Netherlands. *Journal of Geophysical Research: Atmospheres*, *119*, 9654–9665. https://doi.org/10.1002/2014JD021663.1

Gelaro, R., McCarty, W., Suárez, M. J., Todling, R., Molod, A., Takacs, L., & Zhao, B. (2017). The Modern-Era Retrospective analysis for research and Applications, Version 2 (MERRA-2). *Journal of Climate*, *30*(14), 5419–5454. https://doi.org/10.1175/JCLI-D-16-0758.1

Gilbert, K. E. (2016). Eigenfunction approach to the Green's function parabolic equation in outdoor sound: A tutorial. *Journal of the Acoustical Society of America*, *139*(3), 1071–1080. https://doi.org/10.1121/1.4942591

Godin, O. A. (2002). An effective quiescent medium for sound propagating through an inhomogeneous, moving fluid. *Journal of the Acoustical Society of America*, *112*(4), 1269. https://doi.org/10.1121/1.1504853

Haney, M. M. (2009). Infrasonic ambient noise interferometry from correlations of microbaroms. *Geophysical Research Letters*, *36*, L19808. https://doi.org/10.1029/2009GL040179

Herron, T. J., & Tolstoy, I. (1969). Tracking jet stream winds from ground level pressure signals. *Journal of the Atmospheric Sciences*, *26*(2), 266–269. https://doi.org/10.1175/1520-0469(1969)026<0266:TJSWFG>2.0.CO;2

Herron, T. J., Tolstoy, I., & Kraft, D. W. (1969). Atmospheric pressure background fluctuations in the mesoscale range. *Journal of Geophysical Research*, *74*(6), 1321–1329. https://doi.org/10.1029/JB074i006p01321

Jensen, F. B., Kuperman, W. A., Porter, M. B., & Schmidt, H. (2011). *Computational ocean acoustics*. New York: Springer. https://doi.org/10.1007/978-1-4419-8678-8

Kim, K., Rodgers, A., & Seastrand, D. (2018). Local infrasound variability related to in situ atmospheric observation. *Geophysical Research Letters*, *45*, 2954–2962. https://doi.org/10.1002/2018GL077124

Lalande, J.-M., Sèbe, O., Landès, M., Blanc-Benon, P., Matoza, R. S., Le Pichon, A., & Blanc, E. (2012). Infrasound data inversion for atmospheric sounding. *Geophysical Journal International*, *190*(1), 687–701. https://doi.org/10.1111/j.1365-246X.2012.05518.x

Le Pichon, A., Blanc, E., Drob, D., Lambotte, S., Dessa, J. X., Lardy, M., & Vergniolle, S. (2005). Infrasound monitoring of volcanoes to probe high-altitude winds. *Journal of Geophysical Research: Atmospheres*, *110*, D13106. https://doi.org/10.1029/2004JD005587

Le Pichon, A., Blanc, E., & Hauchecorne, A. (2010). *Infrasound monitoring for atmospheric studies*. Springer Science and Business Media.

Le Pichon, A., Vergoz, J., Blanc, E., Guilbert, J., Ceranna, L., Evers, L., & Brachet, N. (2009). Assessing the performance of the International monitoring system's infrasound network: Geographical coverage and temporal variabilities. *Journal of Geophysical Research*, *114*, D08112. https://doi.org/10.1029/2008JD010907

Melton, B. S., & Bailey, L. F. (1957). Multiple signal correlators. *Geophysics*, *22*(3), 565. https://doi.org/10.1190/1.1438390

Olson, J. V. (2004). Infrasound signal detection using the Fisher F-statistics. *InfraMatics*, *6*, 1–7.

Ortiz, H. D., Matoza, R. S., Johnson, J. B., Hernandez, S., Anzieta, J. C., & Ruiz, M. C. (2021). Autocorrelation infrasound interferometry. *Journal of Geophysical Research: Solid Earth*, *126*, e2020JB020513. https://doi.org/10.1029/2020JB020513

Ottemöller, L., & Evers, L. G. (2008). Seismo-acoustic analysis of the Buncefield oil depot explosion in the UK, 2005 December 11. *Geophysical Journal International*, *172*(3), 1123–1134. https://doi.org/10.1111/j.1365-246X.2007.03701.x

Picone, J. M., Hedin, A. E., Drob, D. P., & Aikin, A. C. (2002). NRLMSISE-00 empirical model of the atmosphere: Statistical comparisons and scientific issues. *Journal of Geophysical Research*, *107*(A12), 1468. https://doi.org/10.1029/2002JA009430

Pilger, C., Gaebler, P., Hupe, P., Kalia, A. C., Schneider, F. M., Steinberg, A., & Ceranna, L. (2021). Yield estimation of the 2020 Beirut explosion using open access waveform and remote sensing data. *Scientific Reports*, *11*(1), 1–14. https://doi.org/10.1038/s41598-021-93690-y

Posmentier, E. S. (1967). A theory of microbaroms. *Geophysical Journal International*, *13*(5), 487–501. https://doi.org/10.1111/j.1365-246X.1967.tb02301.x

Posmentier, E. S. (1974). 1- to 16-Hz infrasound associated with clear air turbulence predictors. *Journal of Geophysical Research*, *79*(12), 1755–1760. https://doi.org/10.1029/JC079i012p01755

Scargle, J. D. (1982). Studies in astronomical time series analysis. II. Statistical aspects of spectral analysis of unevenly spaced data. *Acta Pathologica Japonica*, *263*, 835–853. https://doi.org/10.1086/160554

Schwaiger, H. F., Iezzi, A. M., & Fee, D. (2019). AVO-G2S: A modified, open-source ground-to-space atmospheric specification for infrasound modeling. *Computers & Geosciences*, *125*, 90–97. https://doi.org/10.1016/J.CAGEO.2018.12.013

Shani-Kadmiel, S., Assink, J. D., Smets, P. S. M., & Evers, L. G. (2018). Seismoacoustic coupled signals from earthquakes in Central Italy: Epicentral and secondary sources of infrasound. *Geophysical Research Letters*, *45*, 427–435. https://doi.org/10.1002/2017GL076125

Shani-Kadmiel, S., Averbuch, G., Smets, P., Assink, J., & Evers, L. (2021). The 2010 Haiti earthquake revisited: An acoustic intensity map from remote atmospheric infrasound observations. *Earth and Planetary Science Letters*, *560*, 116795. https://doi.org/10.1016/j.epsl.2021.116795

Shumway, R. H. (1971). On detecting a signal in n stationarily correlated noise series. *Technometrics*, *13*(3), 499–519. https://doi.org/10.1080/00401706.1971.10488814

Smart, E., & Flinn, E. A. (1971). Fast frequency-wavenumber analysis and Fisher signal detection in real-time infrasonic array data processing. *Geophysical Journal of the Royal Astronomical Society*, *26*(1–4), 279–284. https://doi.org/10.1111/j.1365-246X.1971.tb03401.x

Smets, P. S. M., Assink, J. D., Le Pichon, A., & Evers, L. G. (2016). ECMWF SSW forecast evaluation using infrasound. *Journal of Geophysical Research: Atmospheres*, *121*, 4637–4650. https://doi.org/10.1002/2015JD024251

Smets, P. S. M., & Evers, L. G. (2014). The life cycle of a sudden stratospheric warming from infrasonic ambient noise observations. *Journal of Geophysical Research*, *119*, 12084–12099. https://doi.org/10.1002/2014JD021905

Smets, P. S. M., Evers, L. G., Näsholm, S. P., & Gibbons, S. J. (2015). Probabilistic infrasound propagation using. *Geophysical Research Letters*, *42*, 6510–6517. https://doi.org/10.1002/2015GL064992.1

Stull, R. (2017). *Practical meteorology: An algebra-based survey of atmospheric science*. University of British Columbia.

Sutherland, L. C., & Bass, H. E. (2004). Atmospheric absorption in the atmosphere up to 160 km. *Journal of the Acoustical Society of America*, *115*(3), 1012. https://doi.org/10.1121/1.1631937

Talmadge, C. L., Waxler, R., Di, X., Gilbert, K. E., & Kulichkov, S. (2008). Observation of low-frequency acoustic surface waves in the nocturnal boundary layer. *Journal of the Acoustical Society of America*, *124*(4), 1956–1962. https://doi.org/10.1121/1.2967474

Thomson, D. J., & Chapman, N. R. (1983). A wide-angle split-step algorithm for the parabolic equation. *Journal of the Acoustical Society of America*, *74*(6), 1848–1854. https://doi.org/10.1121/1.390272

Tolstoy, I., & Herron, T. J. (1969). A model for atmospheric pressure fluctuations in the mesoscale range. *Journal of the Atmospheric Sciences*, *26*(2), 270–273. https://doi.org/10.1175/1520-0469(1969)026<0270:AMFAPF>2.0.CO;2

Vanderbecken, P. J., Mahfouf, J., & Millet, C. (2020). Bayesian selection of atmospheric profiles from an ensemble data assimilation system using infrasonic observations of May 2016 mount Etna eruptions. *Journal of Geophysical Research: Atmospheres*, *125*, e2019JD031168. https://doi.org/10.1029/2019JD031168

Vera Rodriguez, I., Näsholm, S. P., & Le Pichon, A. (2020). Atmospheric wind and temperature profiles inversion using infrasound: An ensemble model context. *Journal of the Acoustical Society of America*, *148*(5), 2923–2934. https://doi.org/10.1121/10.0002482

Vorobeva, E., De Carlo, M., Le Pichon, A., Espy, P. J., & Näsholm, S. P. (2021). Benchmarking microbarom radiation and propagation model against infrasound recordings: A Vespagram-based approach. *Annales Geophysicae*, *39*(3), 515–531. https://doi.org/10.5194/ANGEO-39-515-2021

Waxler, R., & Assink, J. (2019). Propagation modeling through realistic atmosphere and benchmarking. In A. Le Pichon, E. Blanc, & A. Hauchecorne (Eds.), *Infrasound monitoring for atmospheric studies: Challenges in middle atmosphere dynamics and societal benefits* (pp. 509–549). Cham: Springer International Publishing. https://doi.org/10.1007/978-3-319-75140-5_15

Waxler, R., & Gilbert, K. E. (2006). The radiation of atmospheric microbaroms by ocean waves. *Journal of the Acoustical Society of America*, *119*(5), 2651–2664. https://doi.org/10.1121/1.2191607